

GIANT MOLECULAR CLOUDS IN M33
II – HIGH RESOLUTION OBSERVATIONSE. ROSOLOWSKY¹, G. ENGARGIOLA, R. PLAMBECK AND L. BLITZ
Department of Astronomy, University of California, Berkeley, CA 94720*Draft version October 25, 2018*

ABSTRACT

We present $^{12}\text{CO}(1 \rightarrow 0)$ observations of 45 giant molecular clouds in M33 made with the BIMA array. The observations have a linear resolution of 20 pc, sufficient to measure the sizes of most GMCs in the sample. We place upper limits on the specific angular momentum of the GMCs and find the observed values to be nearly an order of magnitude below the values predicted from simple formation mechanisms. The velocity gradients across neighboring, high-mass GMCs appear preferentially aligned on scales less than 500 pc. If the clouds are rotating, 40% are counter-rotating with respect to the galaxy. GMCs require a braking mechanism if they form from the large scale radial accumulation of gas. These observations suggest that molecular clouds form locally out of atomic gas with significant braking by magnetic fields to dissipate the angular momentum imparted by galactic shear. The observed GMCs share basic properties with those found in the Galaxy such as similar masses, sizes, and linewidths as well as a constant surface density of $120 M_{\odot} \text{ pc}^{-2}$. The size–linewidth relationship follows $\Delta V \propto r^{0.45 \pm 0.02}$, consistent with that found in the Galaxy. The cloud virial masses imply that the CO-to-H₂ conversion factor has a value of $2 \times 10^{20} \text{ H}_2 \text{ cm}^{-2}/(\text{K km s}^{-1})$ and does not change significantly over the disk of M33 despite a change of 0.8 dex in the metallicity.

Subject headings:

1. INTRODUCTION

Many theories address molecular cloud formation, but few observations can distinguish between them. As a result, there is little consensus on which process dominates (Elmegreen 1993, and references therein). One avenue for testing these theories is to study molecular clouds in a wide range of environments and to determine which aspects of the environment set the cloud properties. We have adopted this approach in a study of the Local Group galaxy M33. Engargiola et al. (2003, Paper I) completed a survey of the entire optical disk of M33 in $^{12}\text{CO}(J = 1 \rightarrow 0)$ with sufficient sensitivity to detect all molecular clouds more massive than $1.5 \times 10^5 M_{\odot}$. This survey represents the first *flux-limited* survey of giant molecular clouds (GMCs) in any spiral galaxy. While there are complete surveys of molecular gas in the Milky Way, blending of emission along the line of sight make it impossible to obtain a complete catalog. The only other flux-limited survey of a molecular cloud population in another galaxy was completed by the NANTEX group studying the Large Magellenic Cloud (Mizuno et al. 2001). Wilson & Scoville (1990) used the OVRO interferometer to study M33 GMCs at high resolution (20 pc), but their observations were limited to clouds in the central 1.5 kpc of the galaxy that are associated with optical extinction and bright single-dish CO detections.

This paper is a high resolution follow-up to the survey of Paper I, targeting fields known to contain bright GMCs over a large range of galactic radii. The $13''$ observations presented in Paper I have sufficient linear resolution (50 pc) to resolve the emission into molecular clouds, but not to measure the cloud sizes. The higher resolution observations presented here (20 pc) resolve most of the

GMCs, and provide additional information about their masses, angular momenta and morphologies. These data show that the GMCs in M33 are similar to those found in the Milky Way. In addition, the data constrain cloud formation theories, and they suggest that the CO-to-H₂ conversion factor is constant across the galaxy.

2. OBSERVATIONS

2.1. *Interferometer Observations*

We observed 17 fields in ^{12}CO ($J = 1 \rightarrow 0$) using the BIMA array (Welch et al. 1996) in Fall 2000 and Spring 2001. We chose fields that contain the highest mass GMCs cataloged in Paper I (Figure 1). The observations were made in the C-array configuration yielding a synthesized beam FWHM of $\sim 6''$. We observed the CO line in the upper sideband with a velocity resolution of 1.016 km s^{-1} . System temperatures typically ranged between 420 K and 730 K. Table 1 lists the field center, synthesized beam size, integration time, and rms noise for each field. We tried to obtain $< 0.2 \text{ Jy beam}^{-1}$ rms noise in each field while maintaining good UV coverage. Three additional fields (Fields 18 through 20 in Table 1) were observed in conjunction with the survey presented in Paper I and are discussed in more detail in that paper. Because of the longer integration times and smaller synthesized beam sizes, the high resolution observations can detect lower mass clouds than the survey in Paper I.

Our data reduction followed the algorithm developed for the BIMA Survey of Nearby Galaxies (Regan et al. 2001). Only the C-array data were used in producing the final data cubes because of their significantly lower noise levels. Observations of Uranus (Fall 2000) and Mars (Spring 2001) were used to establish the flux of the phase calibrator 0136+478 (3.6 Jy in Fall 2000, 2.7 Jy in Spring 2001). Bootstrapping the quasar flux to the M33 data established the flux calibration. Binning veloc-

¹ eros@astro.berkeley.edu

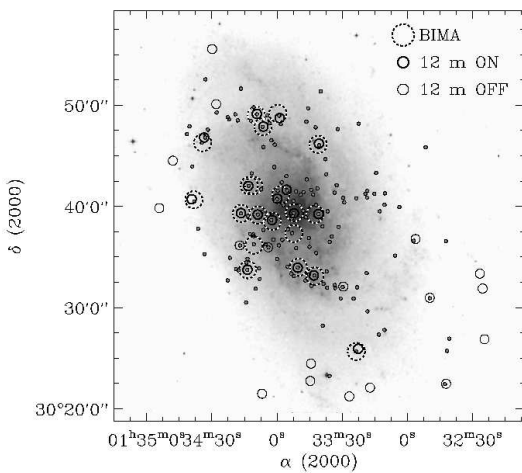


FIG. 1.— The locations of the 20 fields observed by the BIMA interferometer and the 18 locations observed by the UASO 12-m overlaid on smoothed I band DSS image of the galaxy. The locations of the catalog sources from Paper I are plotted as grey circles and were used to target the C-array and 12-m observations.

TABLE 1
OBSERVATIONS OF 20 FIELDS IN M33 USING THE BIMA
MILLIMETER INTERFEROMETER.

Field Name	α (2000)	δ (2000)	Beam Size (")	Source Time (hours)	σ^a (Jy beam $^{-1}$)
1	1 ^h 34 ^m 12 ^s .7	30° 42' 2".80	5.3 \times 5.1	8.22	0.127
2	1 ^h 34 ^m 8 ^s .76	30° 39' 8".78	5.8 \times 5.4	0.872	0.199
3	1 ^h 34 ^m 6 ^s .57	30° 47' 50".8	5.7 \times 5.4	0.872	0.200
4	1 ^h 33 ^m 23 ^s .5	30° 25' 39".8	5.8 \times 4.9	0.255	0.205
5	1 ^h 33 ^m 41 ^s .0	30° 46' 7".43	5.8 \times 5.2	1.34	0.159
6	1 ^h 34 ^m 38 ^s .2	30° 40' 38".1	5.8 \times 5.2	1.34	0.160
7	1 ^h 33 ^m 50 ^s .1	30° 33' 58".3	5.8 \times 5.2	1.34	0.161
8	1 ^h 34 ^m 10 ^s .7	30° 42' 2".80	6.4 \times 5.4	1.88	0.178
9	1 ^h 33 ^m 42 ^s .5	30° 33' 6".61	5.7 \times 5.0	4.44	0.0912
10	1 ^h 34 ^m 2 ^s .20	30° 38' 31".1	6.9 \times 4.9	2.34	0.212
11	1 ^h 34 ^m 13 ^s .5	30° 33' 44".2	6.5 \times 6.0	1.33	0.262
12	1 ^h 33 ^m 51 ^s .9	30° 39' 22".8	6.5 \times 6.0	1.33	0.261
13	1 ^h 34 ^m 34 ^s .2	30° 46' 16".7	6.6 \times 6.3	1.45	0.221
14	1 ^h 33 ^m 59 ^s .6	30° 49' 10".8	6.5 \times 6.0	2.20	0.213
15	1 ^h 34 ^m 16 ^s .4	30° 39' 18".1	6.7 \times 6.2	1.92	0.196
16	1 ^h 34 ^m 10 ^s .5	30° 36' 10".0	6.5 \times 5.8	3.09	0.234
17	1 ^h 34 ^m 9 ^s .50	30° 49' 1".20	6.7 \times 6.1	16.0	0.0832
18 ^b	1 ^h 33 ^m 58 ^s .3	30° 41' 6".99	6.6 \times 6.6	4.00	0.155
19 ^b	1 ^h 33 ^m 42 ^s .5	30° 39' 13".0	6.6 \times 6.5	4.00	0.153
20 ^b	1 ^h 33 ^m 52 ^s .2	30° 37' 19".0	6.6 \times 6.5	4.00	0.155

^aFor a 2 km s $^{-1}$ channel.

^bThese observations of these fields are discussed in Paper I.

ity channels set the final velocity resolution at 2.00 km s $^{-1}$. We used uniform weighting of the UV data in the inversion, choosing a grid spacing that resulted in 1.5" pixels for the final maps, and we cleaned the cube using a Högbom algorithm after correcting for the primary beam attenuation.

2.2. Single Dish Observations

Since interferometers filter out zero-spacing flux from the observed object, complete flux recovery requires additional observations using a single dish telescope. To measure the total flux from the GMC fields, we observed 18 fields over the course of three nights using the University of Arizona Steward Observatory 12-m telescope at Kitt Peak. The selected fields for the 12-m observations are displayed in Figure 1. To check for faint emission, each field was observed to attain a signal-to-noise ratio at the peak of the CO line of at least 10. Every two hours, Jupiter or Saturn was observed to optimize the pointing and focus of the telescope. During sunset, the pointing and focus checks were done before observing each new field to compensate for rapid variations in the thermal stresses on the telescope. Both polarizations were observed with the 500-kHz and 1-MHz filter banks in parallel mode. The median system temperature was 350 K for the observations and the median column of water was 0.7 mm.

The observations used absolute off positions which targeted low-significance detections in the D-array survey (see Paper I). These observations help to establish the completeness limit in the survey by determining the fraction of real detections of low significance. The positions of the off fields were selected to be well separated in velocity from the strong molecular cloud emission in the on position. Emission in the off fields appears as absorption features in the resulting spectra. Only two of the off fields contained emission at the expected velocities.

We reduced the data by flagging bad channels in every spectrum, combining the polarizations to reduce the noise, and fitting a quadratic baseline. The vane calibration of the antenna temperature was found to be accurate to better than 10% using continuum observations of Jupiter and line observations of DR21(OH). All spectra were observed to an rms noise level of at most 10 mK in a 2.6 km s $^{-1}$ channel, equivalent to a molecular gas surface density of of $0.1 M_{\odot}$ pc $^{-2}$.

Finally, we observed a 5×5 pointing mosaic centered on the most massive cloud complex in the galaxy (Field 17 in Table 1) to map all flux associated with this cloud. The single dish map was combined with both the C and D array BIMA data using MIRIAD's imcomb routine. The difference between the fully-recovered data cube and the cube generated solely from the interferometer data shows the location and spatial structure of the emission that is detected only by the 12-m telescope.

2.3. Flux Recovery

By comparing the interferometer and single dish data, we estimate the amount of flux that has been resolved out by the interferometer or not selected by our cloud identification techniques (§2.4). We compare each of the 18 single dish spectra to a representative spectrum generated from the interferometer data by averaging together the spectra in the data cube and correcting for the beam profile of the 12-m. To improve the signal to noise in the interferometer spectrum, only pixels with significant ($> 2\sigma$) CO emission are included in the average. Both the C-array observations and the D-array observations discussed in Paper I recover less than 100% of the flux as expected. The median ratios of the interferometer and

single dish integrated intensities (L_{CO}) are:

$$\langle L_{\text{CO,C}}/L_{\text{CO,12-m}} \rangle = 0.53^{+0.22}_{-0.09} \text{ and}$$

$$\langle L_{\text{CO,D}}/L_{\text{CO,12-m}} \rangle = 0.62^{+0.30}_{-0.13}.$$

Because the distribution of this ratio is asymmetric about its median, we quote the positive and negative dispersions separately. The 12-m observations indicate that a significant fraction of emission is resolved out or masked out (see §2.4). However, comparing the peak antenna temperatures in the spectra shows that:

$$\langle T_{\text{A,C}}/T_{\text{A,12-m}} \rangle = 0.77^{+0.22}_{-0.17} \text{ and}$$

$$\langle T_{\text{A,D}}/T_{\text{A,12-m}} \rangle = 0.89^{+0.11}_{-0.13},$$

while the widths of the interferometer lines are narrower:

$$\langle \Delta v_{\text{CO,C}}/\Delta v_{\text{CO,12-m}} \rangle = 0.71^{+0.22}_{-0.12} \text{ and}$$

$$\langle \Delta v_{\text{CO,D}}/\Delta v_{\text{CO,12-m}} \rangle = 0.72^{+0.25}_{-0.16}.$$

Three effects can lead to a discrepancy between the interferometer and single dish data: (1) calibration errors, (2) extended CO emission resolved out by the interferometer, and (3) limited sensitivity or masking effects in the interferometer data.

Calibration discrepancies would appear as a relative scaling of the observed spectra by a constant factor. However, the ratios of the peak temperatures and linewidths indicate better flux recovery in the middle of the line. We conclude that scaling alone cannot not be the source of flux loss.

Observations of the off positions using the 12-m telescope indicate that there is no extended CO emission on kiloparsec scales with sufficient surface brightness to account for the discrepancy between the interferometer and the single dish observations. Each of the 18 single dish spectra have a 3σ noise level of 0.07 K km s^{-1} ($0.3 M_{\odot} \text{ pc}^{-2}$); however, accounting for the observed difference requires a surface brightness of 1.0 K km s^{-1} ($4.3 M_{\odot} \text{ pc}^{-2}$). To search for even fainter emission, we averaged together the 16 empty off positions, shifting the velocities to align any faint emission at the H I velocity. No line is present in the resulting spectrum, which has a 3σ surface brightness sensitivity of $0.019 \text{ K km s}^{-1}$ ($0.08 M_{\odot} \text{ pc}^{-2}$). Since the off positions are separated by projected distances of roughly a kiloparsec, we conclude that a CO emission component on this scale can account for no more than 2% of the discrepancy between the interferometer and the single dish fluxes.

The extra emission detected in the single-dish spectra is likely from low mass clouds surrounding each GMC lying below our clipping threshold. Figure 2 compares the map of Field 17 generated from interferometer data alone with the map generated by merging interferometer data with the single dish map. The greyscale image is the fully recovered map and the contours represent the *additional* emission seen only in the fully recovered map. The relative levels of the contours to the greyscale are indicated at the bottom of the scale bar, showing the additional flux recovered is a very low surface brightness component. Taking the Fourier transform of the added emission shows that $> 80\%$ of the added flux would be detected by the interferometer with more integration time. The spatial filtering of the interferometer occurs only at UV distances of $< 5k\lambda$ and does not account for the discrepancy between the two telescopes. Most of the added

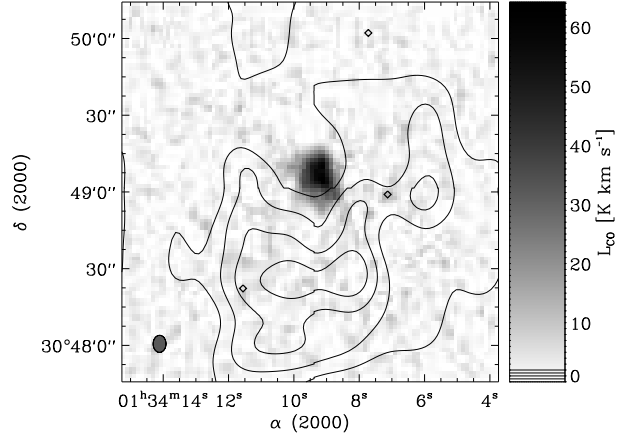


FIG. 2.— Map of emission in Field 17 of the interferometer observations. The greyscale shows the map generated by combining the interferometer and single-spacing data. The contours show the distribution of flux present in the combined map but not in the interferometer map. The contours are spaced at 0.5 K km s^{-1} starting at 0.5 K km s^{-1} , approximately 1σ for this map. The relative levels of the contours are indicated as lines on the scale bar, showing the diffuse emission is of low surface brightness. The three diamonds overplotted are the locations of additional clouds found in deep C-array integrations.

emission is excluded from the interferometer map simply by virtue of being below the significance threshold for our masking methods. Also plotted in Figure 2 are the locations of low mass clouds seen only in the C-array data, where the synthesized beam is well matched to the cloud sizes. Two of these clouds appear in the distribution of diffuse emission suggesting clumpy structure within this envelope. The diffuse emission seems principally associated with the GMCs, and a discussion of what this observation implies for cloud formation appears in §4.4. We conclude that the interferometer observations detect the central clouds of complexes in the galaxy containing high mass GMCs ($M > 1.5 \times 10^5 M_{\odot}$, Paper I).

2.4. Cloud Identification

We defined clouds in the position-velocity interferometer data cubes as connected regions in three dimensions containing more than 50 pixels, each with a value greater than $2\sigma_{\text{rms}}$. Our criteria guarantee that *at least* five statistically independent regions are included in each cloud because interferometer data cubes are oversampled by a factor of 3 in each spatial direction, though the velocity channels are nearly independent. For five joint 2σ detections, the likelihood of false detection is 5×10^{-4} in these data cubes which have $\sim 10^5$ independent elements. Analysis of the noise in the data indicates that the distribution is sufficiently Gaussian to justify such a treatment. We simulated 10^3 UV data sets mimicking the observation conditions, correlator configuration, and baselines of the array. The cloud extraction program found no false detections for these selection criteria.

This algorithm extracts 45 molecular clouds from the data cubes, including all clouds in these fields cataloged in Paper I. To account for low amplitude signal at the edges of the clouds, the regions were expanded by 1 pixel in both the position and the velocity directions. Figure

3 shows maps of the individual clouds. Five of the 45 clouds are not completely recovered since they lie near the half power point of the primary beam. Because their peaks are included in the maps, we estimate that the truncation will not increase their masses and areas by more than a factor of 2.

3. GMC PROPERTIES

The observed parameters of the 45 clouds are listed in Table 2. The analysis uses a distance to M33 of 850 kpc (Kennicutt 1998).

3.1. Cloud Masses

We measure the GMC masses using two methods: (1) assuming a constant CO-to-H₂ conversion factor and (2) applying the virial theorem. The CO-to-H₂ conversion factor (X , Bloemen et al. 1986) converts between integrated CO line intensity (L_{CO}) and molecular hydrogen column density ($N(\text{H}_2)$). We use a conversion factor of

$$X = 2 \times 10^{20} \frac{N(\text{H}_2)/\text{cm}^{-2}}{L_{\text{CO}}/\text{K km s}^{-1}}$$

(Strong & Mattox 1996; Dame et al. 2001). In converting the column density to a cloud mass, we include the mass of helium with a number fraction of 9% relative to hydrogen nuclei. This gives the luminous mass of the cloud:

$$\frac{M_{\text{CO}}}{M_{\odot}} = 4.3 \left(\frac{X}{2 \times 10^{20}} \right) \left(\frac{L_{\text{CO}}}{\text{K km s}^{-1}} \right) \left(\frac{A_{\text{cl}}}{\text{pc}^2} \right), \quad (1)$$

where A_{cl} is the projected surface area of the molecular cloud. Our observations typically have $\sigma_{\text{rms}} = 1.0 \text{ K km s}^{-1}$ ($4.3 M_{\odot} \text{ pc}^{-2}$). Errors in measuring masses using the X factor arise not only from the uncertainty in the X factor but also from the flux calibration and the noise in the data. Determining the true masses of entire GMCs is further complicated by the presence of low surface brightness emission around the central clouds.

For the 36 resolved clouds, we can also compute the mass using the virial theorem. The virial mass requires a measurement of the velocity width of the GMC and the cloud size. We used the intensity-weighted second moments of the position and the velocity to determine the size and linewidth respectively, following Solomon et al. (1987, hereafter S87). The radius of the cloud r is defined as

$$r = 1.36 \sqrt{\sigma_{\alpha}^2 + \sigma_{\delta}^2 - 2\sigma_{bm}^2} \quad (2)$$

where σ_{α} and σ_{δ} are the dispersions in right ascension and declination converted to projected distance and σ_{bm} is the beam width. The coefficient scales the result to match the definitions of cloud radius given in S87 to facilitate comparison with Milky Way GMCs (§4.2). The scaling is chosen so that the radius of a circular cloud would be the same using either measurement method. Our size measure is independent of the orientation of the coordinate system in which the moments are calculated. With the noise level of our data, this radius measurement works best for cloud radii larger than 10 pc, the projected beam radius. With this definition of r , the virial mass of the cloud is then:

$$M_{\text{VT}} = 1427 \left(\frac{\sigma_v^2}{\text{km s}^{-1}} \right) \left(\frac{\sqrt{\sigma_{\alpha}^2 + \sigma_{\delta}^2 - 2\sigma_{bm}^2}}{\text{pc}} \right). \quad (3)$$

This virial mass estimate implicitly assumes a density profile of $\rho \propto r^{-1}$. These methods reproduce the virial masses found by Wilson & Scoville (1990) to within 40% for the four clouds that are well-resolved in both samples.

The virial mass estimate assumes a spherically symmetric cloud so that the velocity dispersion in the radial direction corresponds to the size scale in the plane of the sky. Therefore, the most reliable virial mass estimates come from clouds that appear round on the sky. We define the spatial filling fraction f as

$$f \equiv \frac{4A_{\text{cl}}}{\pi \ell_{\text{max}}^2} \quad (4)$$

which compares the area actually occupied by the cloud to the area that the cloud would occupy if it were circular with diameter equal to ℓ_{max} , the cloud's largest linear dimension. We restrict analyses involving virial masses to the 29 “round” clouds, defined as having $f > 0.5$, to minimize errors in the virial mass estimates. Clouds with small filling fractions appear as elongated structures and suggesting that they may be decomposed into multiple, dynamically distinct GMCs (e.g. Clouds 5, 10, 19, or 21 in Figure 3). Figure 4 compares the virial and luminous (X factor) masses for the 36 resolved clouds in our study. A linear fit between the virial and CO masses for the 29 round clouds finds $M_{\text{VT}} = (1.0 \pm 0.1)M_{\text{CO}} - (0.1 \pm 0.2) \times 10^4 M_{\odot}$ with a reduced χ^2 value of 0.9. The slope of unity implies that our adopted value for the X factor is consistent with the virial masses.

In §2.3, we found that our observations underestimated the integrated intensity and linewidth of the CO emission by 50% and 25% respectively. Recovering more of the flux with higher sensitivity observations would increase the luminous mass as well as the size and linewidth used in the virial mass. These increases tend to offset each other so the ratio of the luminous mass to the virial mass remains roughly constant. To investigate how omitting 50% of the flux in a field affects our mass estimates, we modeled the clouds as azimuthally symmetric brightness distributions with a power law surface brightness ($L_{\text{CO}}(r) \propto r^{\omega}$). The linewidth scales with the size following the relation found in §4.2. Using the above methods, we calculated $M_{\text{CO}}/M_{\text{VT}}$ for the central 50% of the emission and for the entire cloud. For all values of ω between -2 and 0, the ratio for the central 50% is never more than 1.5 times higher than the ratio for the entire cloud. This estimate is an upper limit since some of the emission is likely from dynamically distinct, low mass clouds surrounding each GMC, implying the interferometer recovers significantly more than half the emission from the central cloud. We conclude that there is a good correspondence between virial and luminous masses derived from the interferometer data.

The values of masses, radii and linewidths, are comparable to those found in the Milky Way (S87). The empirical relations between these quantities also match those found for the Milky Way molecular clouds and this similarity is discussed in detail in §4.2.

3.2. Velocity Gradients

The high resolution CO observations allow measurement of the velocity gradient across the molecular clouds. Many mapping studies of Milky Way molecular clouds

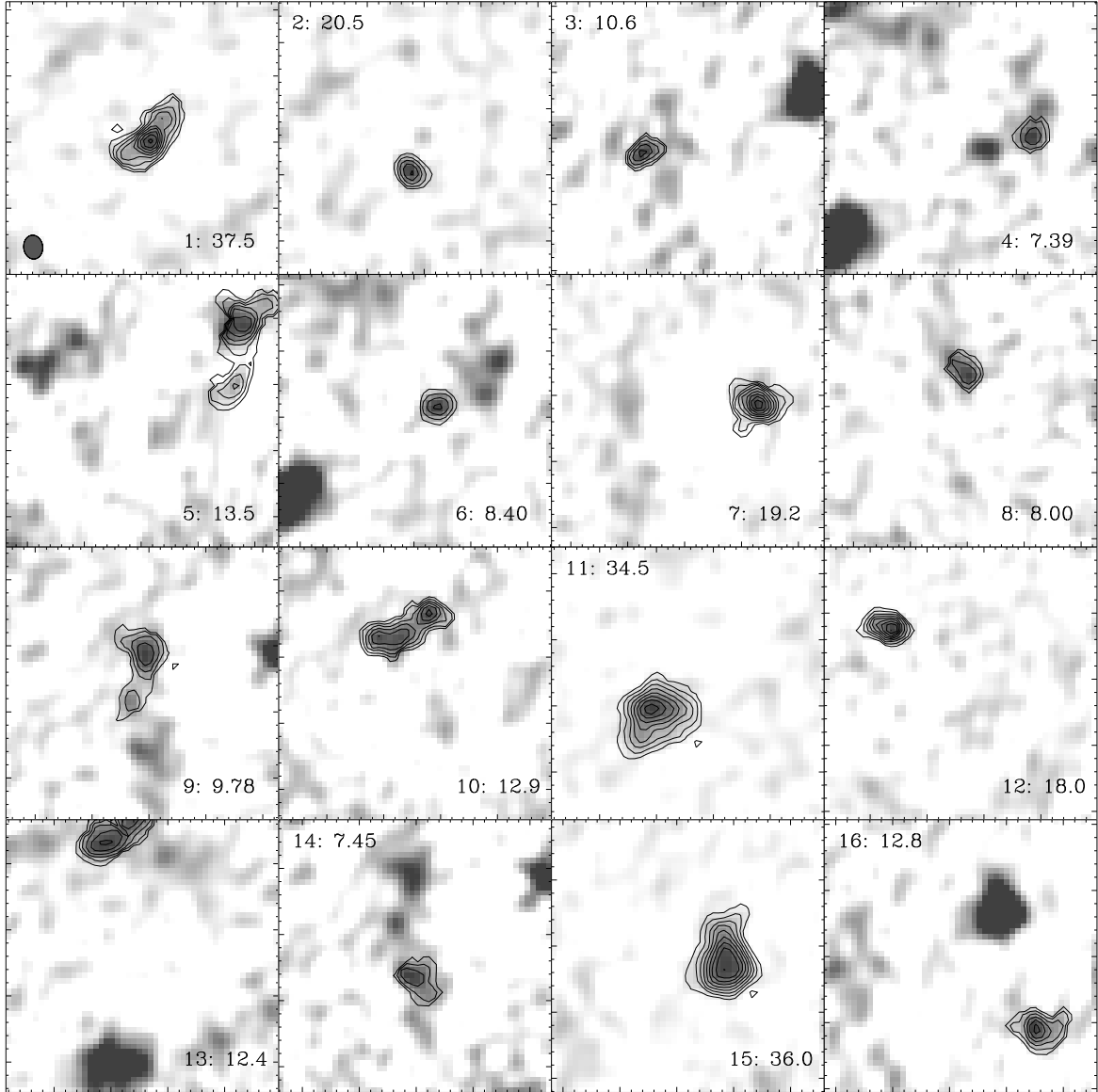


FIG. 3.—Maps of individual molecular clouds in M33. The greyscale map is the CO brightness, integrated over all velocities contributing to the cloud. Each box is 300 pc square. The maps are annotated in the corner with “ $N:L_{\text{CO}}$ ” where N is the number of the cloud in Table 2 and L_{CO} is the peak integrated intensity (K km s^{-1}) in the cloud which sets the top of the greyscale. The bottom of the greyscale is set at 0 K km s^{-1} . Other clouds in the same field of view with higher peak intensities appear saturated. The typical beam is plotted in the first panel of the figure. Plotted over the greyscale are contours of integrated intensity for the cloud under consideration. The spacing between the contours is 2 K km s^{-1} ($\sim 2\sigma_{\text{rms}}$) if the peak integrated intensity (L_{CO}) is less than 20 K km s^{-1} and 4 K km s^{-1} otherwise. The maps show a wide variety of morphologies and brightnesses.

note such gradients and are summarized in Phillips (1999). The clouds in M33 also show significant velocity gradients, with magnitudes comparable to Milky Way clouds. To measure the gradient, we derive the velocity centroid at each position in the cloud using the intensity weighted first moment of the masked spectrum. Then, we fit a plane to the resulting velocity centroid surface. The coefficients of the fit define ∇v_c , the gradient in this surface and v_r , the radial velocity of the cloud, after Goodman et al. (1993). The vector quantity ∇v_c can also be expressed as the gradient magnitude, $|\nabla v_c|$, and the position angle of the gradient ϕ_{cloud} . The latter is measured east from north to facilitate comparison with the orientation of the galaxy. Errors in quantities derived

from the fit are propagated from the original data using the covariance matrix.

The results of the gradient fits are given in Table 2. Planes are good fits to the velocity centroid surfaces with the median value of reduced $\widetilde{\chi^2} = 1.4_{-0.7}^{+2.2}$ for the measured gradients. Fitting other functions (like paraboloids or radial collapse profiles) to the centroid surface yield significantly higher values of $\widetilde{\chi^2}$. The magnitudes of the gradients are displayed in the histogram in Figure 5. The magnitudes are comparable to the typical $0.1 \text{ km s}^{-1} \text{ pc}^{-1}$ for the clouds found in the Milky Way (Blitz 1993; Phillips 1999). In addition, there is no significant relation between position angle and gradient magnitude.

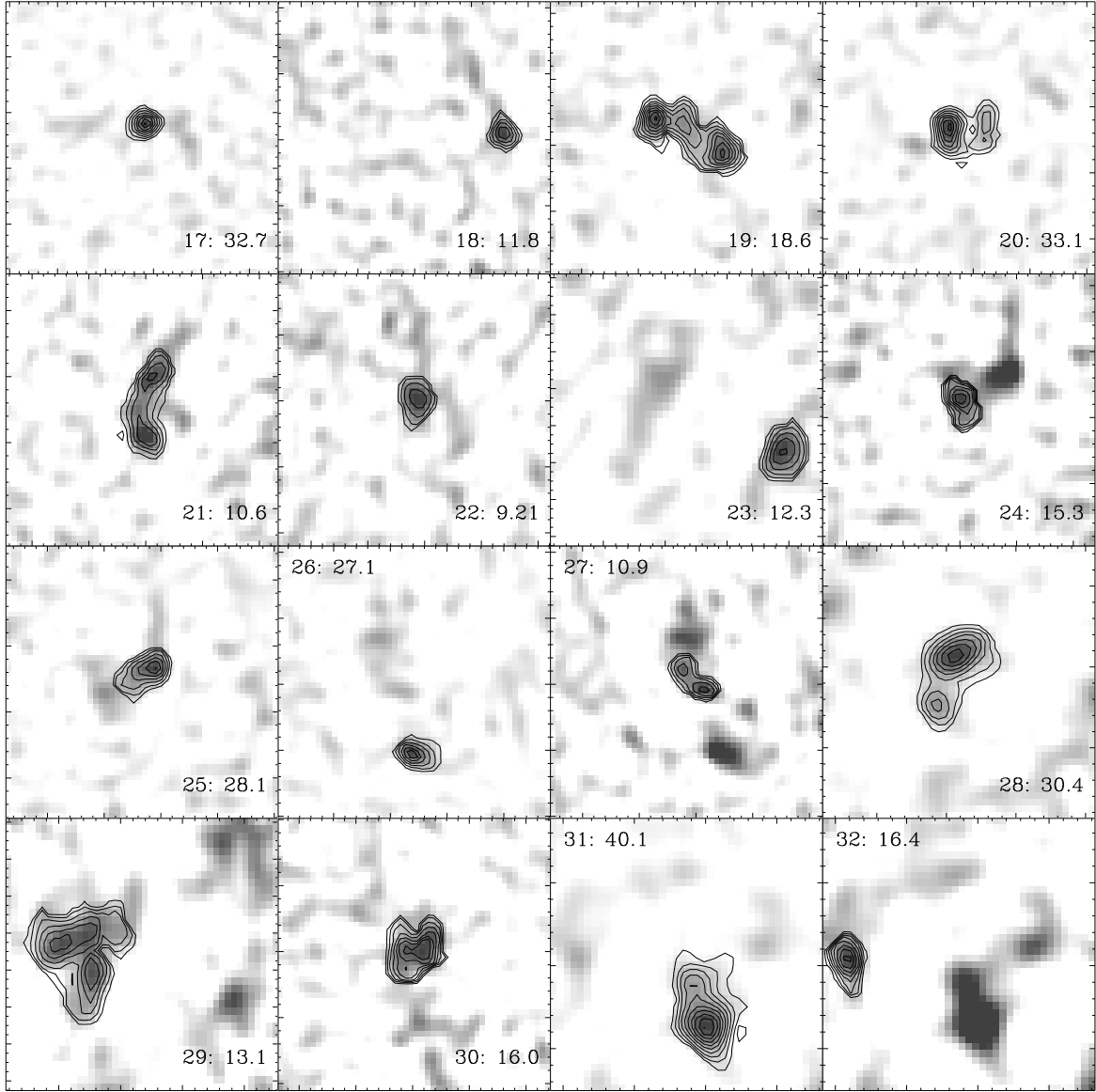
FIG. 3.— *Continued*

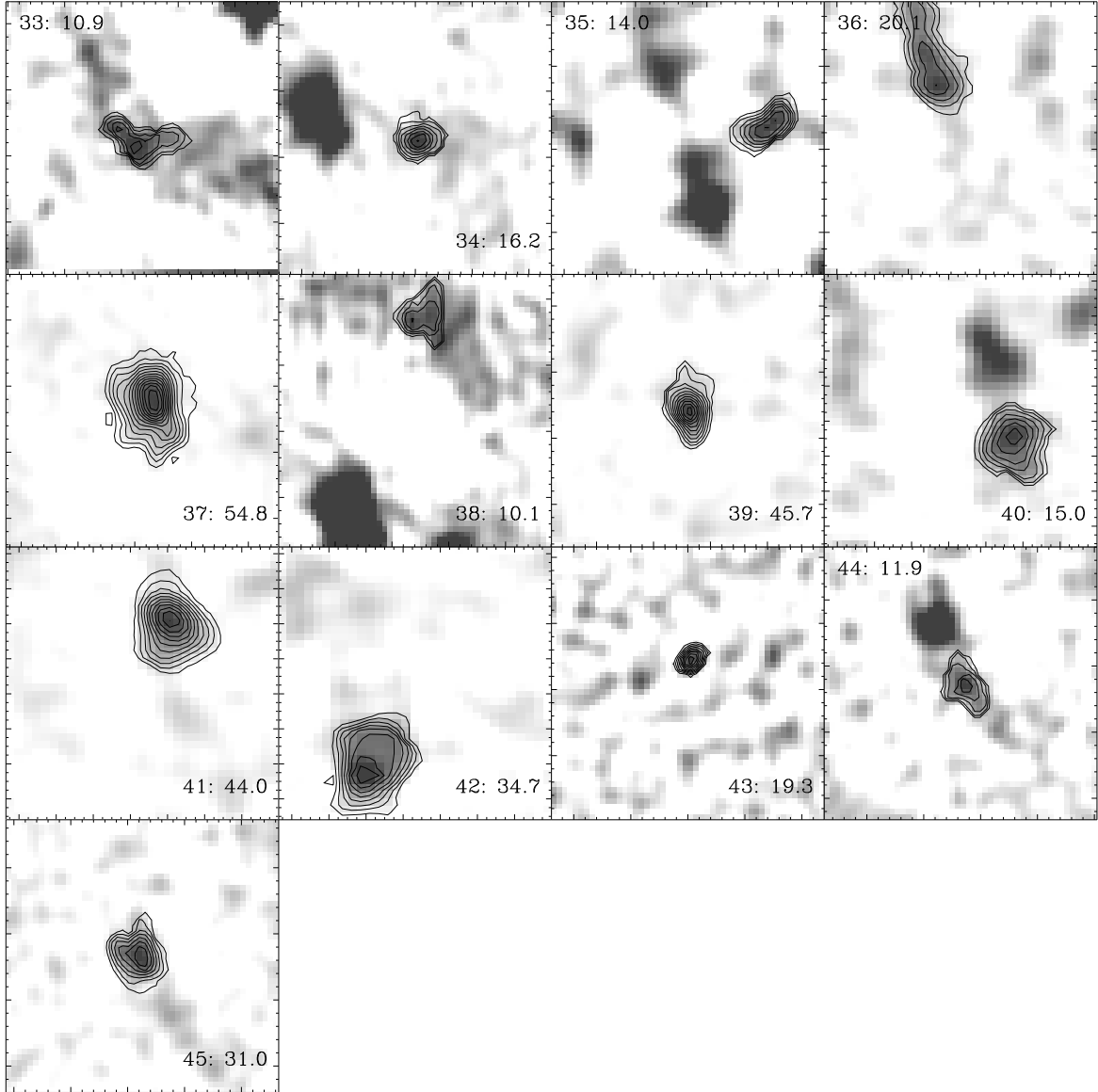
Figure 6 shows position-velocity cuts along the derived gradients for four clouds in the data set. Adjacent to each plot is a position-velocity cut perpendicular to the derived gradient. This figure demonstrates that planes are good fits to the data since the cut along the gradient shows a linear trend and the perpendicular cuts appear constant.

Most authors assume that the velocity gradients are the signature of cloud rotation (Blitz 1993; Phillips 1999). If the gradients are due to rotation, then the magnitude of the velocity gradient measures the angular velocity vector Ω projected into the plane of the sky $|\nabla v_c| = |\Omega| \sin i$. The position angle of the gradient is $\phi_{\text{cloud}} = \phi_\Omega + 90^\circ$. The gradient therefore provides much information about the angular velocity and rotation axis of a cloud. We find (1) the *linear* gradients observed are the signature of *solid-body* rotation. (2) The rotation energy for these clouds is $\lesssim 5\%$ of the cloud binding en-

ergy. (3) The position angles of the rotation axes show marginal alignment with the axis of the galaxy, as is seen in Figure 7. (4) There are many clouds with position angles separated by more than 90° from that of the galaxy. (5) If the clouds are rotating, roughly 40% of the clouds are retrograde rotators (§4.1.4). (6) For the median gradient magnitude of $0.05 \text{ km s}^{-1} \text{ pc}^{-1}$, the rotation period of a molecular cloud would be 125 Myr, significantly longer than the assumed molecular cloud lifetimes of 10 to 30 Myr (Paper I, Blitz 1993).

We measure the angular momentum of the molecular clouds from the gradient fits and the cloud radii. For a solid body rotator with a power law surface mass density, the specific angular momentum² $j = J/M = \beta |\nabla v_c| r^2$

² Through the remainder of the paper, we will refer to the specific angular momentum as the angular momentum. Any case where the true angular momentum, $J = jM$, is intended will be specifically noted.

FIG. 3.— *Continued*

where β is a constant set by the mass profile and r is the radius of the cloud. For a constant surface density cloud, $\beta = 0.4$, ranging from 0.33 to 0.5 for different density profiles (Phillips 1999). This analysis adopts $\beta = 0.4 \pm 0.1$. The derived angular momentum is listed as j_1 in Table 2. The alignment of the rotation axis with respect to the observer affects the magnitude of the observed gradient. The value $j_1 = j \sin i$ where j is the true angular momentum of the cloud and i is the inclination to the line of sight. Without knowing the inclination, j_1 will underestimate the true angular momentum. To avoid assuming solid-body rotation, we calculated a second measurement of the angular momentum

$$j_2 = \sum_{i,j,k} T_A(x_i, y_j, v_k) [(x_i - x_0)^2 + (y_j - y_0)^2]^{1/2}.$$

$$(v_k - v_0) \sin \vartheta_{i,j} \cdot \left[\sum_{i,j,k} T_A(x_i, y_j, v_k) \right]^{-1} \quad (5)$$

where x_0 , y_0 , and v_0 , are the centers of the cloud averaged over position and velocity space respectively and $\vartheta_{i,j}$ is the angle between the point (x_i, y_j) in the cloud and the gradient judged from the center of the cloud. This value can be calculated even when the cloud is too small to be deconvolved accurately. Even with this measurement, a cloud can be oriented with its angular velocity vector along the line of sight thereby obscuring any signature of rotation. The effects of inclination must ultimately be dealt with statistically under the assumption that the clouds are not preferentially oriented towards the observer.

Burkert & Bodenheimer (2000, BB00) show that turbulent velocity fields can also produce linear gradients in the observational domain. The required turbulent power

TABLE 2
CLOUD PROPERTIES FOR CLOUDS FOUND IN M33

Cloud Number	$(\alpha, \delta)^a$ (",")	Alternative ^b Names	V_{LSR} (km s $^{-1}$)	V_{FWHM} (km s $^{-1}$)	r^c (pc)	M_{VT}^c ($10^4 M_{\odot}$)	M_{CO}^c ($10^4 M_{\odot}$)	$ \nabla v ^c$ (0.01 km s $^{-1}$ pc $^{-1}$)	ϕ_{∇}^c ($^{\circ}$)	j_1^c pc km s $^{-1}$	j_2 pc km s $^{-1}$
1	19, -18	EPRB19, WS1,2,4,5	-168.	7.7	27.	31.	26.	8.38	178	19.2	25.3
2	29, -36	EPRB132, WS3	-149.	5.5	—	—	6.7	2.29	-64	—	2.14
3	-82, -41	WS33,34	-162.	6.7	—	—	3.6	9.58	-82	—	6.18
4	71, 100	EPRB31, WS29	-215.	6.1	22.	16. ^d	4.2	10.1	-44	15.3	47.4
5	61, 119	EPRB31, WS29	-223.	11.	48.	100 ^d	14.	13.6	-60	93.9	103.
6	81, 92	EPRB30, WS30	-214.	4.9	—	—	2.9	11.9	19	—	10.3
7	-9, -129	WS10	-151.	8.4	13.	17.	9.9	8.36	143	4.00	13.4
8	26, -117	EPRB75, WS6	-158.	4.9	—	—	2.9	3.49	-33	—	2.44
9	27, -129	EPRB75, WS8,9	-152.	4.4	13.	4.6	5.3	2.20	-9	1.06	4.22
10	113, 115	EPRB18, WS27,28	-221.	6.5	33.	27. ^d	12.	1.90	-16	6.43	8.87
11	119, 69	EPRB3, WS21,22,23(?)	-210.	9.6	32.	56.	41.	9.53	24	30.0	46.0
12	52, -113	EPRB16	-168.	7.6	—	—	6.7	10.6	32	—	12.8
13	118, 133	—	-208.	7.2	22.	22.	11.	3.29	-46	5.06	4.56
14	25, -157	EPRB75, WS7	-153.	4.2	6.7	2.3	3.7	7.70	-91	1.04	12.6
15	-127, -22	EPRB4, WS32	-166.	10.	31.	61.	45.	9.57	-67	27.5	45.6
16	-138, -57	—	-165.	5.5	13.	7.3	7.0	1.25	119	0.617	1.64
17	153, -58	EPRB46, WS16,17,18	-182.	8.2	3.8	4.8	12.	14.0	-4	0.624	16.2
18	249, 145	—	-224.	6.0	—	—	3.4	4.70	-176	—	3.08
19	-4, -340	EPRB20	-134.	4.8	49.	22. ^d	23.	0.685	52	4.99	0.0282
20	233, -26	EPRB7	-195.	6.0	14.	9.4	15.	8.74	-17	4.96	10.5
21	-99, -386	EPRB22	-119.	5.8	42.	27. ^d	12.	4.40	137	24.2	20.4
22	291, 144	EPRB58	-210.	4.6	10.	4.0	5.5	6.75	93	2.04	10.4
23	290, -28	EPRB72	-196.	5.1	—	—	6.2	7.77	-123	—	11.2
24	211, 490	EPRB10	-258.	4.2	14.	4.7	6.7	4.05	-5	2.47	4.75
25	201, 496	EPRB10	-256.	6.7	18.	15.	15.	7.24	-109	7.26	13.9
26	-136, 358	EPRB15	-213.	7.2	7.8	7.7	8.5	11.9	-140	2.24	12.0
27	-129, 378	EPRB15	-216.	6.0	16.	11.	5.5	1.54	112	1.16	4.96
28	256, -199	EPRB6	-160.	6.5	32.	25.	27.	3.49	-24	10.7	6.92
29	330, -19	EPRB21	-191.	7.4	38.	40.	21.	8.91	-170	40.0	47.0
30	-129, 395	EPRB15	-220.	7.3	26.	26.	16.	9.44	-157	19.3	33.9
31	103, 547	EPRB2	-243.	6.5	29.	23.	32.	3.58	-86	9.06	17.6
32	132, 559	—	-244.	5.2	—	—	5.8	4.76	63	—	4.31
33	268, 526	EPRB74	-246.	8.5	28.	38. ^d	8.0	5.35	-55	12.4	18.7
34	211, 562	—	-253.	7.4	8.8	9.2	7.5	13.8	69	3.29	16.7
35	90, 562	—	-246.	5.4	7.9	4.3	6.2	9.35	-135	1.77	19.1
36	115, 579	—	-253.	6.7	47.	41. ^d	24.	3.96	-54	26.9	45.8
37	238, 570	EPRB1	-248.	9.6	38.	67.	78.	7.37	24	33.3	27.6
38	218, 625	EPRB108	-249.	6.8	16.	14.	7.1	9.67	116	8.03	14.6
39	295, -352	EPRB5	-157.	9.0	21.	32.	32.	7.47	-110	9.61	29.3
40	548, 413	—	-248.	6.2	13.	9.3	9.6	7.93	-144	3.85	12.8
41	552, 431	EPRB8	-242.	8.7	19.	27.	28.	6.97	175	7.66	11.4
42	564, 403	EPRB9	-222.	9.3	23.	38.	30.	8.22	-130	13.7	28.3
43	-362, -821	—	-74.0	6.3	—	—	4.6	9.95	-104	—	7.18
44	618, 48	EPRB11	-202.	6.4	18.	14.	6.7	10.8	-30	10.7	23.4
45	627, 65	EPRB11	-204.	9.2	23.	38.	25.	8.56	32	14.4	19.2

^aRight ascension and declination are given in seconds of arc relative to the galactic center at $\alpha_{2000} = 1^{\text{h}}33^{\text{m}}50^{\text{s}}8$ and $\delta_{2000} = 30^{\circ}39'36.7'$.

^bNames are those found in Wilson & Scoville (1990), denoted WSXX where XX is the cloud number in Table 2 of their paper and those found in Paper I, denoted EPRBXX where XX is the number in that paper. Clouds referred to twice are clouds resolved into two separate clouds by higher angular resolution.

^cProperties are derived using methods described in text. Approximate errors are $\delta r = 5$ pc, $\delta M_{\text{VT}} = 20\%$, $\delta M_{\text{CO}} = 40\%$, $\delta |\nabla v| = 0.02$ km s $^{-1}$ pc $^{-1}$, $\delta \phi = 10^{\circ}$, $\delta j_1 = 0.03$ pc km s $^{-1}$.

^dFilling fraction (f , Equation 4) is less than 0.5, so the virial mass estimate is unreliable.

spectrum, $P(k) \propto k^n$, has a value of n between -3 and -4 , so that the largest size-scales have the most power, appearing as gradients. Using their scaling for the magnitude of the velocity gradient as a function of size gives gradients on order 0.08 km s $^{-1}$ pc $^{-1}$ for the median cloud radius of 20 pc, comparable to the observed values. If the gradients are due to turbulence and not rotation, our measurements change only in that the angular momentum derived from the data will *overestimate* the true value of the angular momentum by a factor of 2 to 3

(BB00). The orientation of the net angular momentum vector is still represented by the position angle of the gradient.

4. DISCUSSION

4.1. Angular Momentum Constraints on GMC Formation

The measured angular momenta are significantly less than expected from simple theories of cloud formation. In the absence of external forces, the angular momentum

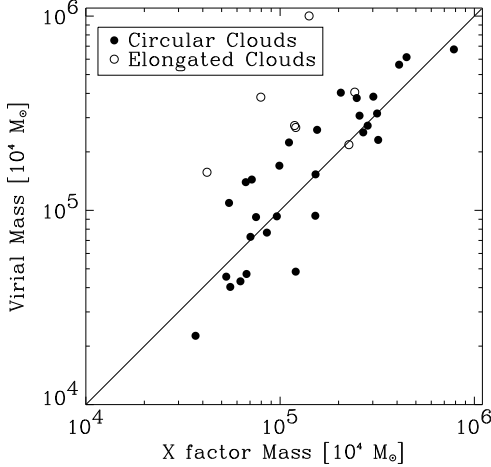


FIG. 4.— Comparison of virial and luminous masses. Elongated clouds are those with a spatial filling fraction less than 0.5. Errors for M_{VT} are $\pm 30\%$ and for M_{CO} are $\pm 40\%$. The solid line indicates the locus where $M_{VT} = M_{CO}$. Clouds with a spatial filling fraction greater than 0.5 show good agreement between their virial masses and the masses derived from the X factor with $X = 2 \times 10^{20} \text{ H}_2 \text{ cm}^{-2} / (\text{K km s}^{-1})$.

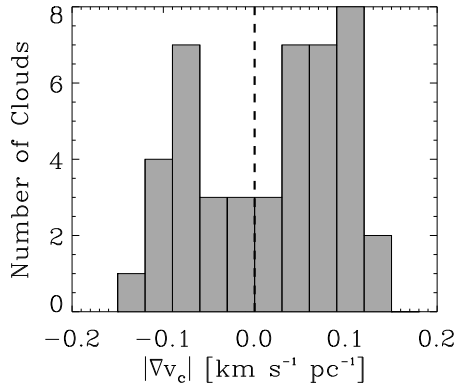


FIG. 5.— Histogram of gradient magnitude values for clouds in M33. Negative values are given to those clouds that have a position angle differing from the galaxy by more than 90° . The gradient magnitudes are comparable to typical values found in the Milky Way. Moreover, the magnitudes of the gradients are comparable among clouds independent of alignment with the galaxy.

of a molecular cloud should be equal to the angular momentum of the gas from which it formed. In a shearing galactic disk, the initial angular momentum for a forming cloud is (see Appendix A):

$$j_{gal} = \eta \frac{1}{R_c} \frac{d}{dR} (RV) \bigg|_{R=R_c} \Delta R^2. \quad (6)$$

In this equation, R is the distance from the center of the galaxy, R_c is galactocentric radius where the cloud is found, and $V(R)$ is the galactic rotation curve (from Corbelli & Schneider 1997). The radial accumulation length ΔR is half the radial extent of the parent atomic

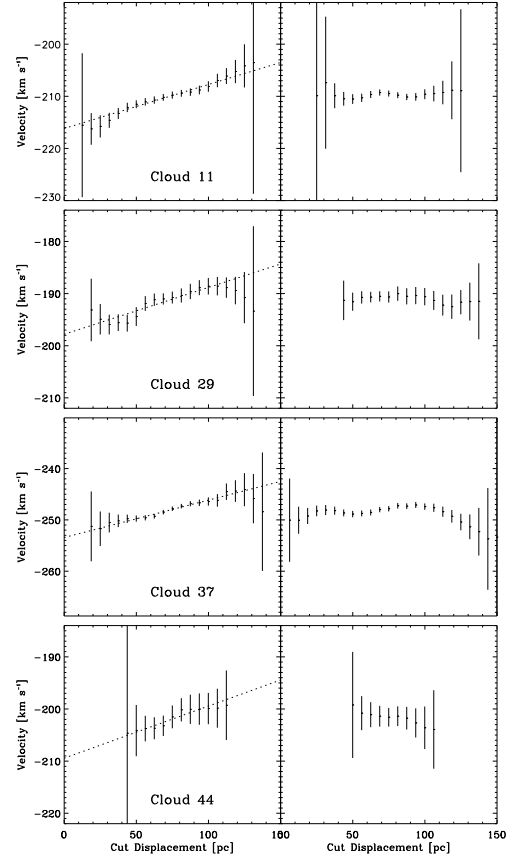


FIG. 6.— Examples of four fitted gradients for molecular clouds observed with C-array. The left-hand column contains plots of the velocity centroids denoted by 1σ error-bars from a position-velocity cut along the direction of the gradient. The dotted line is a linear fit to the gradient. The right hand column is identical to the left column, except the position-velocity cut is made perpendicular to the gradient. The minimal curvature in the left column and zero slope in the right indicate that planes are good fits to the velocity centroid surfaces.

gas. The radial mass distribution of the collapsing gas determines the parameter η .

In the simplest case, the radial accumulation length is set by requiring the mass of atomic hydrogen in a cylinder stretching to infinity in the z direction and of radius ΔR to equal the mass of the molecular cloud: $\Sigma_{\text{HI}} \cdot \pi \Delta R^2 = M_{\text{GMC}}$. We adopt $\eta = 1/4$ in Equation 6 calculated for the collapse of a cylinder. Using the measured masses of molecular clouds and the local value of Σ_{HI} , we find that *in all but 3 of the 36 resolved molecular clouds, the predicted angular momentum is higher than the observed value, on average by a factor of 5*. We calculated the values of Σ_{HI} using the maps of Deul & van der Hulst (1987) after recalibrating this map to match the surface density of Corbelli & Schneider (1997). If the velocity gradients are due to turbulence instead of rotation, BB00 argue that the observed angular momentum should be scaled down by a factor of 2 to 3, which only increases the discrepancy between the predicted angular momentum and the observed value. Statistically, projection effects can account for only 20% of the discrepancy.

We refine this simple model as follows: (1) by assum-

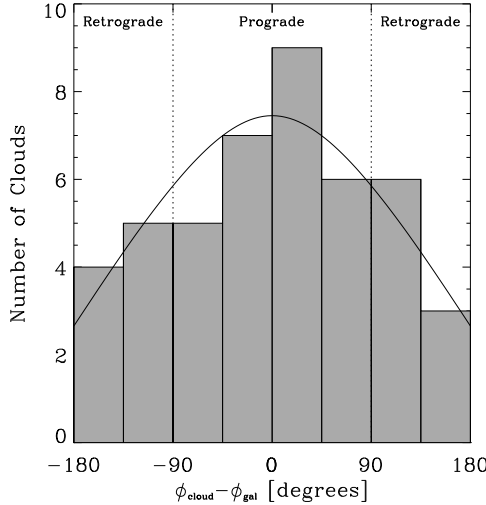


FIG. 7.— Histogram of the position angles of the GMC rotation with respect to that of the galaxy. Clouds show slight preferential alignment with the orientation of the galaxy. The line represents the predicted distribution for a value of $\alpha = 0.69$ in Equation 9. Rough separations between Prograde and Retrograde clouds are shown, but the unknown inclinations of the clouds prevent this separation from being completely determined.

ing that the gas far from the galactic plane does not contribute to the forming molecular cloud and (2) by including some estimate of projection effects. Instead of the progenitor material extending infinitely far from the galactic plane, we assume the gas is accumulated over a cylinder with its height equal to its diameter, centered on the location of the GMC. The three-dimensional distribution of atomic hydrogen is unknown, but we assume a scale height of $H = 100$ pc throughout the galaxy with $\rho(z) \propto \text{sech}^2(z/2H)$. Changing this value by a factor of 2 does not alter the results significantly. Again, the dimensions of the cylinder are determined by requiring its volume to contain a mass of atomic gas equal to that of the molecular cloud. Using the radius of the cylinder as the radial accumulation length ΔR , the predicted angular momentum is determined from Equation 6. We also assume the clouds are solid body rotators with random orientations and scale the predicted angular momentum down by a factor of $\langle \sin i \rangle = \pi/4$. If, instead, we assume the clouds are strictly aligned with the galaxy, the correction only differs from $\pi/4$ by 3%. We compare this model to the measurements in Figure 8. The measured angular momenta are plotted as $\pm 1\sigma$ error bars as a function of galactic radius. Figure 8 shows that the observations are always less than the predictions of this Solid Body Model (filled circles). The discrepancy is more than an order of magnitude for 20 of the clouds.

4.1.1. The Toomre and Parker Instabilities

Recent work on star formation at galactic scales suggests that star formation preferentially occurs where the gas disk is Toomre unstable (Martin & Kennicutt 2001). We calculate the radial accumulation length if the clouds actually formed from the instability. The Toomre (1964) instability is a gravitational instability in a shearing, thin

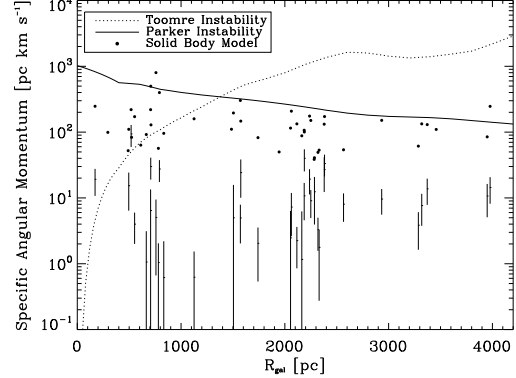


FIG. 8.— Specific angular momenta (j_1) imparted by different collapse mechanisms as a function of galactic radius. The measurements are represented by $\pm 1\sigma$ error bars. The two curves are the imparted angular momenta as a function of R_{gal} for the Toomre and Parker Instabilities. The filled points are the predicted values of the specific angular momentum for the solid body rotator discussed in the text. Nearly all measurements of the specific angular momentum lie well below the predictions for all models.

fluid disk that bunches the gas into concentric rings, provided the disk is unstable according to the criterion

$$\frac{\kappa \sigma_v}{\pi G \Sigma(R)} < 1 \quad (7)$$

where κ is the local epicyclic frequency, σ_v is the (three dimensional) velocity dispersion of the fluid, and $\Sigma(R)$ is the local surface mass density of the fluid under consideration. The radial accumulation length is set by the original radial extent of the contracting rings:

$$\Delta R_T = \frac{2\pi^2 G \Sigma(R)}{\kappa^2} = \frac{\lambda_T}{2}, \quad (8)$$

where λ_T is the most unstable scale for Toomre collapse. The rotation curve determines the epicyclic frequency for the galaxy

$$\kappa^2 = 2 \left(\frac{V^2}{R^2} + \frac{V}{R} \frac{dV}{dR} \right)$$

We assume that there is sufficient mass in the annulus to form molecular clouds which is true over most of the galaxy.

Figure 8 also shows the predicted values of the cloud angular momentum for GMCs formed using the Toomre instability. These values only agree with the observed angular momenta for a few clouds in the inner 500 pc of the galaxy, *where the disk is most stable* according to the criterion in Equation 7. Since all but two of the clouds disagree with the predictions of the Toomre instability by a large margin, it seems unlikely that the clouds form by the action of this instability alone. Moreover, the Toomre instability predicts that cloud angular momentum should increase with galactocentric radius, which is not seen in Figure 8.

The Parker instability is another potential avenue of molecular cloud formation (Mouschovias *et al.* 1974; Elmegreen 1982; Hanawa *et al.* 1992). The Parker instability is a magneto-hydrodynamic (MHD) effect in gas coupled to a buoyant magnetic field. As the instability evolves, a section of the field bulges out of the plane of

the galaxy, causing the atomic gas to flow down the gravitational potential well along the edge of the bulge and collect into molecular clouds. The characteristic length scale of the instability is $\lambda_P \approx \pi H$, where H is the scale height (Giz & Shu 1993). The values for the predicted angular momentum are shown in Figure 8, for a 100 pc scale height. These values have been corrected for the pitch angle of the magnetic field ($\theta = 60^\circ$, Beck 2000) since the collapse occurs along the magnetic field lines, so that $\Delta R_P = (\lambda_P \sin \theta)/2$. The Parker instability also gives a large discrepancy between the observed and predicted values. Matching the observed values would require a gas scale height of ~ 20 pc, which would imply an unrealistically large stellar mass density.

4.1.2. The Angular Momentum Problem

We conclude *none of the simple theories produce the observed values of angular momentum in the molecular clouds*. Figure 8 compares the theoretical and observed angular momentum for the resolved molecular clouds. Even using the moment based measurement of angular momentum (j_2), we find an average discrepancy of more than a factor of 5 between observation and theory. This discrepancy shows that nearly all clouds suffer an angular momentum problem independent of assuming solid-body rotation. The failure of the Solid Body Model is particularly troubling since this model gives the minimum accumulation length required to gather the mass of the GMC from the atomic hydrogen. This constraint will limit even the most sophisticated models of cloud formation.

There are at least two possible solutions to the angular momentum problem. One is to gather material for molecular clouds from similar galactocentric radii, thereby minimizing the shear in the atomic gas, as may happen in the swing amplification instability (Kim & Ostriker 2001). If clouds have small radial accumulation lengths, they must have long azimuthal accumulation lengths. Agreement with the observed angular momenta requires $\Delta R < 30$ pc. To form a cloud of $10^5 M_\odot$ out of atomic hydrogen with a typical surface density of $7 M_\odot \text{ pc}^{-2}$ requires azimuthal accumulation lengths of ~ 500 pc. With the maximum non-circular velocities in the atomic gas $\lesssim 10 \text{ km s}^{-1}$ (Deul & van der Hulst 1987), this implies a limit on the timescale of cloud formation of $\tau_{\text{form}} \gtrsim 50$ Myr, larger than the 10–20 Myr cloud lifetimes implied in Paper I. This timescale is a significant fraction of the time between the spiral arm crossings for most of the galaxy away from the co-rotation radius (Newton 1980). Consequently, such a long time scale for cloud formation has difficulties explaining preferentially finding clouds in spiral arms of galaxies.

A second solution is to brake the material with external forces such as magnetic fields. Magnetohydrodynamic effects seem to be critical for shedding angular momentum in the star formation process and may also act in the early stages of cloud formation. If the magnetic field is so dynamically significant as to produce an instability, it may also provide enough tension to brake the clouds during their formation. Beck (2000) measures the mean field strength in M33 as $6 \pm 2 \mu\text{G}$, which gives an Alfvén speed of $\sim 6 \text{ km s}^{-1}$ (assuming a sech^2 density profile to calculate the midplane volume mass density). This value is comparable to the sound speed in the warm neutral

medium of most galaxies, suggesting that MHD braking and cloud formation via instabilities occur on comparable timescales. The braking time is set by the time needed for an Alfvén wave to sweep through a volume of diffuse gas with a moment of inertia equal to that of the forming cloud (Mestel & Paris 1984). If the atomic gas has a constant density, then the Alfvén wave must pass through a distance comparable to the accumulation length for the molecular cloud. Instabilities cause cloud formation on a time scale comparable to the sound crossing time for the accumulation length. Since the crossing times for sound and Alfvén waves are comparable, we conclude that MHD braking is a viable option to slow the rotation of forming clouds. Because only 10% of clouds show angular momentum approaching the expected values from any of the formation mechanisms (e.g. Figure 8), the MHD braking must occur in the atomic gas or during a small fraction of the molecular cloud lifetime. We return to the implications of these observations for cloud formation in §4.4.

4.1.3. Angular Momentum Magnitude Correlations

The molecular clouds in this sample suggest a correlation between specific angular momentum and mass. Fitting a power-law relationship between j_1 and M_{CO} finds $j(M) \propto M^{0.6 \pm 0.1}$, though there is significant scatter in the data ($\tilde{\chi}^2 = 6.1$, Figure 9). A similar correlation appears in the Milky Way data where Phillips (1999) finds $j \propto M^{0.7}$. If the molecular clouds form by accumulation of atomic gas, then the angular momentum should scale as the accumulation length squared (Equation 6): $j \propto \Delta R^2$. The mass of the cloud is $M = \pi \Delta R^2 \Sigma_{\text{H}_2}$, so a correlation is expected with $j \propto M/\Sigma_{\text{H}_2}$. The variations in the mean hydrogen surface density are small compared to the order of magnitude spanned in mass (§4.2), so the angular momentum is expected to scale with mass for any accumulation model. That $j \propto M^{0.6}$ instead of $j \propto M$ may be due to the action of the braking mechanism, though $j \propto M$ is not strongly ruled out by the poor quality of the fit. Such correlation between j and M is also expected for a turbulent velocity field. BB00 find that the velocity gradient scales with clouds size r as $|\nabla v| \propto r^{-0.5}$ so $j_1 \propto |\nabla v| r^2 \propto r^{1.5}$. The clouds in our sample have a constant surface density regardless of cloud size (§4.2). Therefore, the mass of a cloud is proportional to its area $M \propto r^2$ and $j \propto M^{0.75}$, close to the observed trend.

There is no significant variation of specific angular momentum as a function of galactic radius, contrary to the predictions of all the accumulations mechanisms considered here (Figure 8). This implies that the angular momentum of the clouds does not depend on any of the properties that change across the galactic disk, including galactic shear, surface mass density of stars and atomic gas, interstellar pressure, interstellar radiation field, or metallicity.

4.1.4. Position Angle Correlations

The position angle of the angular momentum vector can be measured from the velocity gradients as discussed in §3.2. The data show correlations between the cloud position angles and that of the galaxy as well as among the individual GMCs. If the angular momentum is set

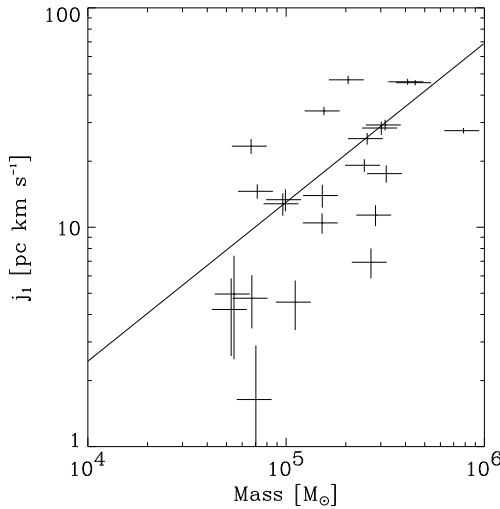


FIG. 9.— The correlation between the magnitude of the specific angular momentum and the mass of the cloud. Only clouds that are well resolved with low filling factors are included in this fit. The solid line is a least-squares, power-law fit to the data with $j_1 \propto M^{0.6 \pm 0.1}$ accounting for errors in both directions.

entirely by the galactic shear, then the rotation axes of the GMCs should be aligned with the galaxy. The distribution of gradient position angles is shown in Figure 7, including rough divisions between prograde and retrograde rotators (assuming the gradients represent rotation). Because of the unknown inclination of the clouds relative to the line of sight, we analyze the distribution of position angles statistically. We assume that the clouds are distributed with orientations on the sphere set by the probability distribution function (PDF):

$$\mathbb{P}(\theta, \varphi) = \frac{1}{2\pi\alpha} \left[\frac{\cos \theta + 1}{2} \right]^{1/\alpha-1} \frac{\sin \theta}{2} \quad (9)$$

where θ is the angle between the angular momentum vector of the cloud and that of the galaxy, α is a parameter that determines the degree of alignment between these vectors, and φ is the azimuthal angle. For $\alpha = 1$, the orientation angles are randomly distributed on the sphere so there are an equal number of prograde and retrograde rotators. For $\alpha \approx 0$, the clouds are closely aligned with the galaxy ($\alpha = 0.2$ implies that 91% of the clouds are prograde rotators). This PDF is motivated solely for ease of simulation so that a single parameter α determines how well aligned the clouds are with the galaxy. By determining the value of α that most closely represents the observed distribution of position angles, we measure the degree of alignment between the clouds and the galaxy. We generated position angle distributions following this PDF using Monte Carlo simulations and then used a one-sided K-S test to measure the difference between the observed and simulated distributions. After testing a range of α , we found the most probable value is $\alpha = 0.69$ (with K-S likelihood $P = 0.99$), implying 61% of the clouds are prograde rotators. The likelihood of a random distribution on the sphere ($\alpha = 1$) is significantly lower ($P = 0.60$) implying some alignment between the clouds and the galaxy. Nevertheless, the wide

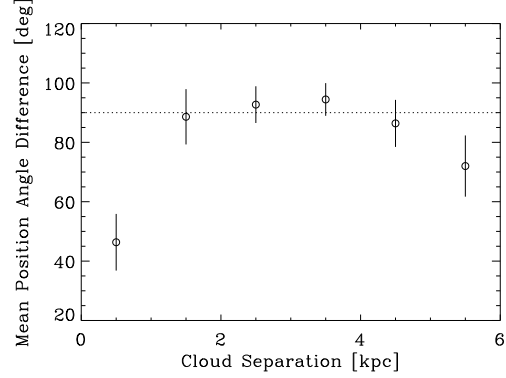


FIG. 10.— The correlation between the position angle of molecular clouds and their separation for clouds with $M > 8 \times 10^4 M_\odot$. There is a trend that clouds at small distances tend to have their velocity gradients aligned with each other. The mean in each bin is weighted according to the uncertainty in the measurements and the error bars are the error in the mean. The first bin is the average of 21 pairs of position angles.

range of position angles indicates any angular momentum imparted by galactic shear is randomized in some fashion.

In addition to the cloud-galaxy correlation, nearby clouds show a higher degree of correlation between their gradient position angles. Figure 10 shows the difference in position angle between pairs of clouds as a function of cloud separation. This figure uses clouds with $M > 8 \times 10^4 M_\odot$ since these clouds have the most significant gradients. If the clouds are randomly oriented with respect to each other, the value of this statistic should be 90° , but clouds with separations smaller than 500 pc show a significantly smaller value implying their angular momentum vectors are aligned. This alignment would be expected if these neighboring clouds formed from the same parent cloud of H I. If clouds are the product of large scale motions in the diffuse ISM, this 500 pc length may represent the scale of the flows that give rise to the clouds.

4.2. Larson's Laws in M33

The clouds in the M33 observations have similar radii ($\sim 20 \rightarrow 50$ pc), masses ($\sim 10^4 \rightarrow 10^6 M_\odot$) and velocity dispersion FWHMs ($5 \rightarrow 10$ km s $^{-1}$) as those found in the Milky Way by S87. We tested these similarities in more detail and found the GMCs in M33 were indistinguishable from those in the Milky Way. We emphasize comparison of our results with the work done by S87 because both studies use equivalent methods for determining the properties of the molecular clouds and the sensitivities are comparable: ~ 0.7 K km s $^{-1}$ for S87 vs. $0.6 \rightarrow 1.3$ K km s $^{-1}$ for this work. We only use the 23 clouds that are well-resolved ($r > 10$ pc) and round ($f \geq 0.5$) in these comparisons since the derived properties of these clouds are the most reliable.

The results of Paper I show that the mass spectrum for GMCs in M33 differs from that found in the Milky Way: $dN/dM \propto M^{-2.6}$ for M33 vs. $dN/dM \propto M^{-1.5}$ for the Milky Way (S87). Despite differences in the mass distribution, clouds in M33 show the same power law relationships between size, mass and linewidth as are seen

in the Milky Way (Larson's Laws, after Larson (1981), see also S87). We plot the size-linewidth and the mass-linewidth relationship for the clouds in M33 in Figure 11 along with the data from the Milky Way (Solomon et al. 1987; Heyer et al. 2001). Where feasible, the cloud properties of the Milky Way data have been recomputed using the methods in §3 to ensure a common basis for comparison. Fitting power-laws to the two relationships shows $\Delta V \propto r^{0.45 \pm 0.02}$ and $M \propto \Delta V^{4.2 \pm 0.3}$. The fits are consistent with the relations seen in the Milky Way (S87) in both normalization and scaling. However, cloud sizes in M33 are systematically smaller by $\sim 30\%$ in M33 compared to S87, which is most likely due to differences in the size measurement technique.

Figure 12 shows the mean surface mass density within molecular clouds as a function of cloud mass. This figure shows no significant scaling of surface density with mass. Similar plots of surface density as a function of cloud radius and galactic radius also show no scaling. The slopes of linear fits between the mass density and cloud mass or cloud radius are consistent with zero. In addition, two statistical tests of correlation, the Spearman rank order and the Kendall τ tests show no significant correlation between mass, radius and surface density (see Press et al. 1992). We conclude that GMCs have a surface mass density of $120 M_{\odot} \text{ pc}^{-2}$ ($2N(\text{H}_2) = 6 \times 10^{21} \text{ cm}^{-2}$) with a dispersion of 60%, which does not vary with cloud mass or radius. This constant mass density is also seen for the GMCs in the Milky Way (Blitz 1993).

The consistency of Larson's laws between the Milky Way and M33 shows that the macroscopic properties of a GMC ($r, \Delta V, N(\text{H}_2)$) are the same in both galaxies for a given cloud mass. Since these macroscopic properties follow similar trends, it is reasonable to expect that the internal properties of GMCs depend only on the mass of the cloud. The GMCs throughout the Local Group also follow Larson's Laws; the LMC (Mizuno et al. 2001), Andromeda (Sheth et al. 2000), and dwarf elliptical galaxies (Young 2001, 2002) all show some evidence that cloud properties are set by cloud mass. Some unifying mechanism must establish the macroscopic properties of the cloud solely in terms of the cloud mass. Since turbulence could provide a relationship between size and linewidth, the balance between turbulent support and self-gravity would naturally set the macroscopic properties of a cloud solely in terms of its mass (Larson 1981; Elmegreen 1989).

4.3. The CO-to-H₂ Conversion Factor

In M33, we are presented with a unique opportunity to study the effects of galactic environment on the CO-to-H₂ conversion factor (X) since there are no systematic differences due to inhomogeneous observation techniques or multiple galaxies. Many studies report a variation in the X factor as a function of metallicity *e.g.* Arimoto et al. (1996) and references therein. There is no evidence for such a trend in M33. In Figure 13, we plot the ratio of the luminous to virial mass $M_{\text{CO}}/M_{\text{V}}$ as a function of metallicity for the 23 well-resolved ($r > 10 \text{ pc}$), round ($f > 0.5$) GMCs in our study. The metallicity at each point is obtained using the position of the cloud and the metallicity gradient ($d[\text{O}/\text{H}]/dR$) of

Henry & Howard (1995). Fitting a line to the data gives:

$$\frac{M_{\text{CO}}}{M_{\text{V}}} = (0.03 \pm 0.23) ([\text{O}/\text{H}] - [\text{O}/\text{H}]_{\odot}) + (0.88 \pm 0.09)$$

accounting for errors in both the metallicity (0.1 dex) and the mass ratio (Press et al. 1992). The value of χ^2 for the fit is 0.9. The value of χ^2 using the relationship of Arimoto et al. (1996, dotted line) as a fit gives 3.31, showing poor agreement ($P = 10^{-5}$) with their quoted trend. The slope of our fit is consistent with *no variation in the conversion factor over a range of 0.8 dex in metallicity* (a factor of 6). Brand & Wouterloot (1995) note that the ratio between virial and CO masses does not change systematically with radius in the Milky Way. In §3.1, we argue that interferometer observations overestimate the ratio $M_{\text{CO}}/M_{\text{V}}$ by *at most* a factor of 1.5. This cannot account for the discrepancy with the Arimoto et al. (1996) data, which we attribute to the difficulties in synthesizing a homogeneous data set from multiple observational studies using a variety of analysis techniques.

The studied GMCs range in galactocentric radius from 170 pc to 4000 pc, and there are significant changes in galactic properties over this range. The interstellar radiation field changes value by nearly an order of magnitude over this range in galactic radius (Walterbos & Greenawalt 1996). Other variations include changes in the cosmic ray flux and the midplane pressure of the gas. Such robustness of the X factor as a GMC mass measure is observed in the Milky Way (S87), but variations among galaxies may still produce different values in the conversion factor. For example, the X factor may change for GMCs in even lower metallicity systems such as the SMC that have an average metallicity below the minimum 8.1 observed in M33.

4.4. Implications for Cloud Formation

This study of M33 suggests several attributes of the molecular cloud formation process. (1) Molecular clouds form directly from atomic hydrogen rather than the agglomeration of small molecular clouds. (2) The formation process makes both low mass and high mass molecular clouds in regions of cloud formation. (3) The formation events are local, *i.e.* length scales less than 500 pc. (4) The progenitor gas has its initial angular momentum dissipated by MHD effects. (5) The similarity of molecular clouds across many environments implies that the molecular mass distribution sets the properties of molecular clouds and star formation.

Our results complement those of Paper I where it is argued that molecular clouds form directly from atomic hydrogen. In that paper, the striking correspondence between molecular clouds and dense atomic filaments strongly suggests cloud formation from atomic gas. This work strengthens that suggestion since we find no evidence for diffuse molecular gas that could serve as a precursor to GMCs (§2.3). Additionally, the atomic gas is significantly more massive than the molecular component on a global as well as a local ($\sim 100 \text{ pc}$) scale. If diffuse molecular gas were the precursor material, the angular momentum problem would be greatly exacerbated, scaling predicted angular momenta up by a factor of $\Sigma_{\text{HI}}/\Sigma_{\text{H}_2, \text{diffuse}} > 20$. We also find that the flux not

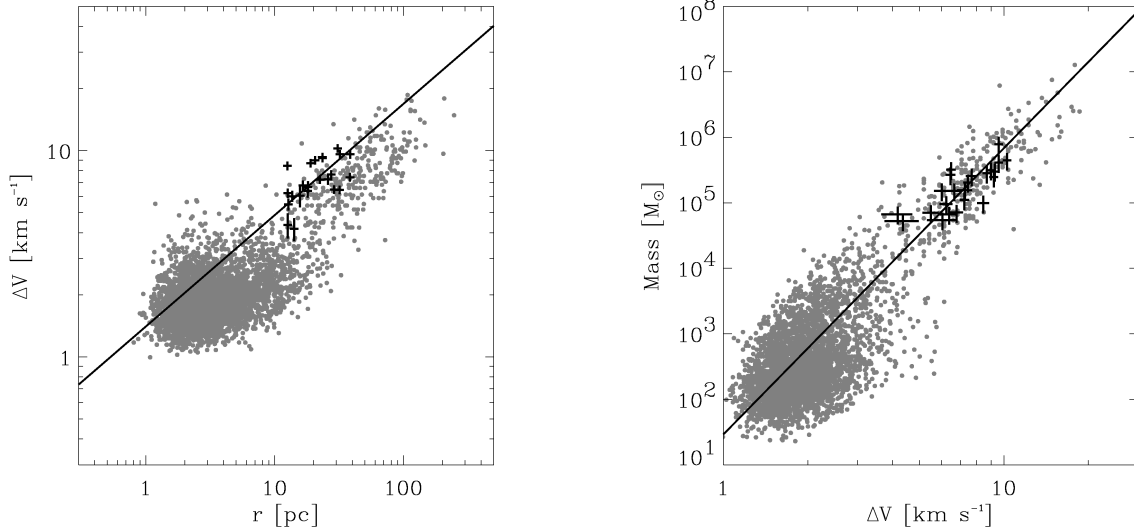


FIG. 11.— The size-linewidth and mass-linewidth radius relationship for the molecular clouds in M33. In both plots, the overlaid grey dots represent the molecular clouds from a Milky Way catalog generated by merging S87 and Heyer *et al.* (2001). The power-law fits give $\Delta V \propto r^{0.45 \pm 0.02}$ and $M \propto \Delta V^{4.2 \pm 0.3}$. The radius measurements for the Milky Way have been recalculated to match the methods discussed in §3, though a slight offset between the data sets persists.

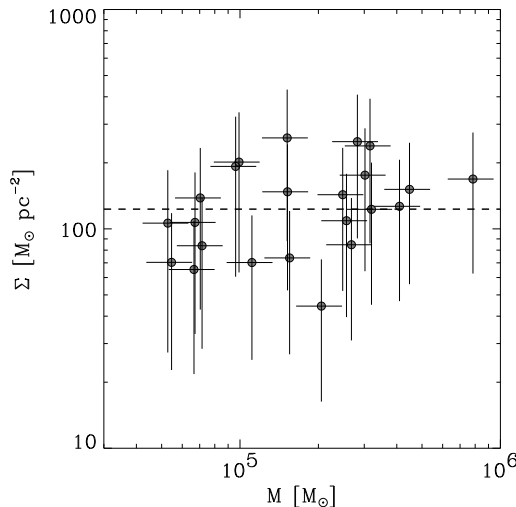


FIG. 12.— Plot of molecular surface density averaged over GMC as a function of mass for 23 well-resolved, round clouds. The surface density is calculated using the deconvolved radius r and the luminous mass M_{CO} . There is no significant scaling with mass. Similar plots as a function of cloud radius and galactic radius also show no scaling. The mean surface density (dashed line) is $120 M_{\odot} \text{ pc}^{-2}$ with a scatter of 60%.

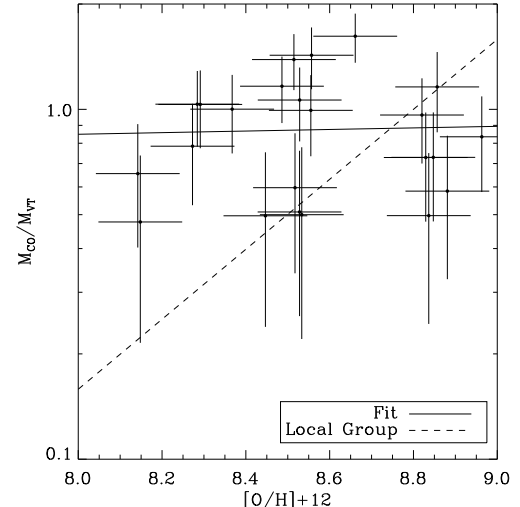


FIG. 13.— Variation of $M_{\text{CO}}/M_{\text{VT}}$ as a function of metallicity for 23 well-resolved, round clouds in M33. A linear regression shows no significant effect from changing metallicities, shown by the solid line. The dashed line plots the trend from Arimoto *et al.* (1996) summarizing similar measurements throughout the Local Group.

recovered in Paper I survey can be accounted for by halos of molecular gas around the detected GMCs, comprised in part by low mass molecular clouds (§2.3). These low mass clouds may form in the same event as the high mass cloud at the center of the interferometer field. Such low mass molecular clouds would have easily been detectable in the off fields of the 12-m observation and may be restricted to regions where high mass molecular clouds also

form.

The position angle correlations in §4.1.4 suggest that the formation of molecular clouds occurs on length scales less than 500 pc. A common formation event could produce aligned molecular clouds, analogous to the formation of the solar system producing aligned rotation in the planets. Correlations in the orientation of angular momentum can be predicted in simulations of turbulent cloud formation that include realistic models of galactic

shear. Such predictions should show the observed degree of alignment with the galaxy and correlations among the GMCs.

The angular momentum problem can be solved by appealing to MHD braking. Forming the molecular clouds from a narrow range of radii requires a long formation time. Formation mechanisms that accumulate gas supersonically cannot have any angular momentum dissipated by Alfvén waves since the accumulation time is smaller than crossing times for magnetosonic waves. In contrast, the magnetic field is sufficient to brake forming molecular clouds and braking occurs over timescales comparable to those of instabilities that could potentially form molecular clouds (§4.1.2).

Molecular clouds appear to have their macroscopic properties (R , ΔV) set by their masses (§4.2). In addition, there appears to be a constant star formation rate per unit molecular mass within galaxies (Wong & Blitz 2002). If this is true, then the properties of star formation on a galactic scale depend on the amount of atomic gas converted into molecular clouds and little else. Although there are similarities in the properties of molecular clouds for a fixed mass, there is good evidence that the mass distribution of molecular gas into individual clouds varies among galaxies. Different mass spectra may be the hallmark of multiple formation mechanisms converting atomic into molecular gas. The steep mass spectrum for the molecular clouds in M33 (Paper I) represents the *only* difference in the molecular cloud population between M33 and the Milky Way. The mass distribution of molecular gas is thus the dominant factor controlling star formation on a local and galactic scale.

5. CONCLUSIONS

We have presented high resolution follow-up observations to a survey of GMCs in M33 made by Engargiola et al. (2003), using the BIMA array and the UASO 12-m millimeter wave telescope. A total of 45 individual GMCs were detected. The UASO 12-m observations measured the total flux in 18 fields, providing information on the flux lost by the interferometer and the presence of a diffuse component of molecular gas. From our observations, we made the following conclusions.

1. There is no evidence for a diffuse molecular component traced by CO spanning the disk of M33. We place a 3σ surface mass density limit of $\Sigma_{\text{H}_2} < 0.3 M_{\odot} \text{ pc}^{-2}$ on the presence of such a component. This is significantly less than the typical surface density of atomic hydrogen, $7 M_{\odot} \text{ pc}^{-2}$.

2. Most of the CO flux in the galaxy is associated with GMCs with smaller clouds clustered around the large cloud. Low mass clouds may appear in other parts of the galaxy but are not ubiquitous.

3. The velocity gradients of the molecular clouds are approximately linear. The magnitudes of the gradients are comparable to those found in the Milky Way. If the gradients are due to rotation, the rotation period is significantly longer than a cloud lifetime (for $\tau_{\text{cloud}} \leq 30$ Myr).

4. GMCs show significantly smaller angular momenta than are predicted by simple formation theories. The discrepancy is, on average, a factor of 5 and ranges up to

two orders of magnitude. If the velocity gradients are due to turbulent motions, the discrepancy widens by at least a factor of 2. Both the Toomre and Parker instabilities predict angular momentum values that are discrepant from observations.

5. The specific angular momentum is related to mass as $j(M) \propto M^{0.6 \pm 0.1}$. This value is consistent with the derived value for the Galaxy of $j \propto M^{0.7}$ (Phillips 1999). There is no significant variation of the specific angular momentum with galactocentric radius, though such variations are predicted by all the large scale accumulation theories.

6. The clouds appear somewhat aligned with the rotation of the galaxy, though a random distribution of position angles is not strongly excluded. If the velocity gradients are from rotation, only $\sim 60\%$ of the clouds are prograde rotators.

7. The projected velocity gradients of neighboring, high-mass clouds are preferentially aligned. This correlation vanishes for separations larger than 500 pc. This alignment may be a signature of the large scale mechanisms that dictate the formation of molecular clouds and should be seen in turbulent cloud formation models.

8. The observed molecular clouds are similar to those found in the Milky Way. We find a size-linewidth relationship of $\Delta V \propto r^{0.45 \pm 0.02}$ and a mass-line width relationship of $M \propto \Delta V^{4.2 \pm 0.3}$. Both of these relationships are indistinguishable from those found in the Milky Way. There is also no detectable variation in the column density of the molecular clouds with the mass or radius of the clouds.

9. Equivalent virial masses and luminous masses imply that the X factor for M33 is equal to $2 \times 10^{20} \text{ H}_2 \text{ cm}^{-2} / (\text{K km s}^{-1})$. There is no significant variation of the X factor with metallicity over a range of 0.8 dex.

10. These observations support a model for cloud formation in M33 using atomic gas as the progenitor material for molecular clouds. The formation process accumulates the atomic gas over a small distance (< 500 pc) with significant braking by magnetic fields.

We thank an anonymous referee whose comments improved the paper. We gratefully acknowledge the help of Edvige Corbelli for the H I surface density and rotation curve data used in her paper. We thank Adam Leroy for extremely useful discussions of data reduction and analysis. Our discussions with Ellen Zweibel regarding MHD braking during cloud formation have proven especially fruitful. Observations at the UASO 12-m were aided by great help from the operator team consisting of Sean Keel, Jon Carlsen, John Downey and headed by Paul Hart. We are also grateful to Tom Dame who provided us with swift checks on our data using the CfA 1.2 m telescope. ER's work is supported in part by a NSF Graduate Fellowship and was completed with great encouragement from Elizabeth Tan. This research has been made possible by extensive use of NASA's Astrophysics Data System (ADS) and the NASA/IPAC Extragalactic Database (NED).

APPENDIX

IMPARTED ANGULAR MOMENTUM

Consider the progenitor mass for a molecular cloud distributed in galactocentric radius with a linear mass density $\lambda(R)$. The specific angular momentum of this material is

$$j = \frac{1}{M} \int \lambda(R) V(R) R \, dR.$$

If the cloud's final distance from the center of the galaxy is R_c , then we define $r \equiv R - R_c$ and perform a Taylor expansion of the velocity curve around R_c to get

$$j = \frac{1}{M} \int \lambda(r) [V_0 + rD(R_c)] (r + R_c) \, dr$$

where

$$D(R_c) \equiv \left. \frac{1}{R} \frac{d}{dR} (VR) \right|_{R=R_c}.$$

Multiplying out the integral gives,

$$j = \frac{1}{M} \left[MV_0 R_c + [R_c D(R_c) + V_0] \int \lambda(r) r \, dr + D(R_c) \int \lambda(r) r^2 \, dr \right]$$

where the first term represents the angular momentum of a particle orbiting the center of the galaxy and the other two terms are the spin angular momentum of the cloud, the measured quantity in these observations. In the absence of external forces, the cloud will collapse to the center of mass, which implies $\int \lambda(r)r = 0$. In this case, the imparted angular momentum is

$$j_{gal} = V_0 R_c + \eta D(R_c) \Delta R^2$$

where the matter is accumulated from a region of width $2\Delta R$. We define a constant η set by the moment of the mass distribution in terms of the dimensionless parameter $u = r/\Delta R$:

$$\eta = \int_{-1}^1 \lambda(u) u^2 \, du. \quad (\text{A1})$$

For collapse in a circular region of radius ΔR around R_c with uniform surface mass density, $\eta = 1/4$.

REFERENCES

Arimoto, N., Sofue, Y., & Tsujimoto, T. 1996, PASJ, 48, 275
 Beck, R. 2000, in The interstellar medium in M31 and M33. Proceedings 232. WE-Heraeus Seminar, 22-25 May 2000, Bad Honnef, Germany. Edited by Elly M. Berkhuijsen, Rainer Beck, and Rene A. M. Walterbos. Shaker, Aachen, 2000, p. 171-178, 171-178
 Blitz, L. 1993, in Protostars and Planets III, 125-161
 Bloemen, J. B. G. M., Strong, A. W., Mayer-Hasselwander, H. A., Blitz, L., Cohen, R. S., Dame, T. M., Grabelsky, D. A., Thaddeus, P., Hermsen, W., & Lebrun, F. 1986, A&A, 154, 25
 Brand, J. & Wouterloot, J. G. A. 1995, A&A, 303, 851
 Burkert, A. & Bodenheimer, P. 2000, ApJ, 543, 822 (BB00)
 Corbelli, E. & Schneider, S. E. 1997, ApJ, 479, 244
 Dame, T. M., Hartmann, D., & Thaddeus, P. 2001, ApJ, 547, 792
 Deul, E. R. & van der Hulst, J. M. 1987, A&AS, 67, 509
 Elmegreen, B. G. 1982, ApJ, 253, 634
 Elmegreen, B. G. 1993, in Protostars and Planets III, 97-124
 Elmegreen, B. G. 1989, ApJ, 338, 178
 Engargiola, G., Plambeck, R., Rosolowsky, E. W., & Blitz, L. 2003, ApJ, submitted (Paper I)
 Giz, A. T. & Shu, F. H. 1993, ApJ, 404, 185
 Goodman, A. A., Benson, P. J., Fuller, G. A., & Myers, P. C. 1993, ApJ, 406, 528
 Hanawa, T., Matsumoto, R., & Shibata, K. 1992, ApJ, 393, L71
 Henry, R. B. C. & Howard, J. W. 1995, ApJ, 438, 170
 Heyer, M. H., Carpenter, J. M., & Snell, R. L. 2001, ApJ, 551, 852
 Kennicutt, R. C. 1998, ApJ, 498, 541
 Kim, W. & Ostriker, E. C. 2001, ApJ, 559, 70
 Larson, R. B. 1981, MNRAS, 194, 809
 Martin, C. L. & Kennicutt, R. C. 2001, ApJ, 555, 301
 Mestel, L. & Paris, R. B. 1984, A&A, 136, 98
 Mizuno, N., Yamaguchi, R., Mizuno, A., Rubio, M., Abe, R., Saito, H., Onishi, T., Yonekura, Y., Yamaguchi, N., Ogawa, H., & Fukui, Y. 2001, PASJ, 53, 971
 Mouschovias, T. C., Shu, F. H., & Woodward, P. R. 1974, A&A, 33, 73
 Newton, K. 1980, MNRAS, 190, 689
 Phillips, J. P. 1999, A&AS, 134, 241
 Press, W. H., Teukolsky, S. A., Vetterling, W. T., & Flannery, B. P. 1992, Numerical recipes in C. The art of scientific computing (Cambridge: University Press, —c1992, 2nd ed.)
 Regan, M. W., Thornley, M. D., Helfer, T. T., Sheth, K., Wong, T., Vogel, S. N., Blitz, L., & Bock, D. C.-J. 2001, ApJ, 561, 218
 Sheth, K., Vogel, S. N., Wilson, C. D., & Dame, T. M. 2000, in The interstellar medium in M31 and M33. Proceedings 232. WE-Heraeus Seminar, 22-25 May 2000, Bad Honnef, Germany. Edited by Elly M. Berkhuijsen, Rainer Beck, and Rene A. M. Walterbos. Shaker, Aachen, 2000, p. 37-40, 37-40
 Solomon, P. M., Rivolo, A. R., Barrett, J., & Yahil, A. 1987, ApJ, 319, 730 (S87)
 Strong, A. W. & Mattox, J. R. 1996, A&A, 308, L21
 Toomre, A. 1964, ApJ, 139, 1217
 Walterbos, R. A. M. & Greenawalt, B. 1996, ApJ, 460, 696
 Welch, W. J., et al. 1996, PASP, 108, 93
 Wilson, C. D. & Scoville, N. 1990, ApJ, 363, 435
 Wong, T. & Blitz, L. 2002, ApJ, 569, 157
 Young, L. M. 2001, AJ, 122, 1747
 —. 2002, AJ, 124, 788